# Generation of Hairpin Vortices Using a Hybrid Physio-Cyber Data Assimilation Approach

Akshit Jariwala\*
The University of Texas at Austin, Austin, TX 78712

John D.B. Wylie<sup>†</sup> Rensselaer Polytechnic Institute, Troy, NY 12180

Alexandros Tsolovikos<sup>‡</sup> The University of Texas at Austin, Austin, TX 78712

Saikishan Suryanarayanan §
The University of Akron, Akron, OH 44325

Efstathios Bakolas  $\P$  The University of Texas at Austin, Austin, TX 78712

Michael Amitay <sup>∥</sup> *Rensselaer Polytechnic Institute, Troy, NY 12180* 

David Goldstein \*\*
The University of Texas at Austin, Austin, TX 78712

Turbulent boundary layers are largely influenced by spatiotemporally developing coherent structures known as Large-Scale Motions (LSMs). This work examines the idea of creating synthetic hairpin trains, a model for LSMs, generated in a nominal zero pressure gradient laminar boundary layer. The study investigates the agreement between the experimentally measured flow field and the hairpin vortices and its simulated counterpart with a hybrid 2D inlet region. This approach uses time-varying unsteady spatially discrete velocity data obtained through experiments as an inflow boundary condition to the direct numerical simulation (DNS). A pre-processing divergence correction and interpolation scheme is employed to convert experimental data into a format better suited for the DNS. The matching is done by recreating a downstream flow using this hybrid physio-cyber approach. This method demonstrates the capability to produce a sequence of hairpins even with a simple 2D planar coarse dataset. A satisfactory qualitative and quantitative agreement was evident when comparing Q-criterion iso-surfaces of instantaneous DNS and phase-locked experimental data. The results of this study not only demonstrate the efficacy of the proposed approach in recreating LSMs but also suggest its applicability to future hybrid experimental-DNS flow control studies.

# I. Nomenclature

 $\lfloor \cdot \rfloor$  = floor function

<sup>\*</sup>Graduate Student, Department of Aerospace Engineering and Engineering Mechanics, The University of Texas at Austin; Corresponding author email: akshit@utexas.edu

<sup>†</sup>Graduate Student, Department of Mechanical, Aerospace, and Nuclear Engineering, Rensselaer Polytechnic Institute

<sup>&</sup>lt;sup>‡</sup>Graduate Student, Department of Aerospace Engineering and Engineering Mechanics, The University of Texas at Austin

<sup>§</sup> Assistant Professor, Department of Mechanical Engineering, The University of Akron

Associate Professor, Department of Aerospace Engineering and Engineering Mechanics, The University of Texas at Austin

Professor, Department of Mechanical, Aerospace, and Nuclear Engineering, Rensselaer Polytechnic Institute

<sup>\*\*</sup>Professor, Department of Aerospace Engineering and Engineering Mechanics, The University of Texas at Austin

 $(\cdot)_x$  = quantity in streamwise direction  $(\cdot)_y$  = quantity in wall-normal direction  $(\cdot)_z$  = quantity in spanwise direction  $dt_{\text{DNS}}$  = non-dimensional timestep for DNS

 $dt_{PIV}$  = non-dimensional timestep for experimental data acquisition

f = actuation frequency

 $h_{sj}$  = synthetic jet orifice cross-sectional width

L = length of computational domain N = number of spectral elements

 $N_{\rm DNS}$  = number of DNS timesteps between each PIV measurement

n = number of PIV data acquisition points

 $Re_{\delta_{in}}$  = Reynolds number based on inlet boundary layer thickness

t = non-dimensional time U = velocity vector [u, v, w]  $U_{\infty}$  = free stream velocity x = streamwise coordinate y = wall-normal coordinate

 $y_{\text{offset}}$  = vertical displacement for experimental data along y axis

z = spanwise coordinate

⊗ = Kronecker product between two matrices

 $\alpha$  = synthetic jet pitch angle

 $\begin{array}{lll} \delta & = & \text{experimental boundary layer thickness} \\ \delta^* & = & \text{experimental displacement thickness} \\ \delta_{\text{in}} & = & \text{DNS boundary layer thickness at inlet} \\ \theta & = & \text{experimental momentum thickness} \\ \nu & = & \text{kinematic viscosity} \end{array}$ 

 $\rho$  = density

# **II. Introduction**

Turbulent boundary layers (TBLs), seemingly chaotic, reveal an underlying order upon closer examination, manifested as spatiotemporally evolving streamwise velocity fluctuations. Large-Scale Motions (LSMs), predominantly residing in the log- and outer layers of turbulent boundary layers, contribute significantly to this order. These LSMs exhibit coherence and substantial correlations over both temporal and finite spatial length scales, influencing the flow by churning as a mechanism to generate turbulence [1]. Spectral analysis of LSMs highlights their substantial contribution to turbulent kinetic energy (TKE) [2], average Reynolds shear stress, and momentum transport within the boundary layer [3–6]. Due to their statistical significance, LSMs have the potential to impact the dynamics of the boundary layer, presenting as organized sequences of hairpin vortices riding either slow- or fast-moving fluid zones [7].

Since LSMs and associated hairpin vortices actively alter the statistics and dynamics of the turbulent boundary layer, they make ideal candidates for selective manipulation. The drag reduction techniques such as Large-Eddy Break Up (LEBU) devices target outer layer coherent structures [8]. Dilute polymers [9] and riblets on the wall surface [10–12] also act as boundary layer control mechanisms. Targeted manipulation of LSMs can potentially increase the wall shear stress and re-energize the boundary layer for separation control. An active flow control strategy could involve identifying these structures, predicting their motion, and targeting them to improve re-attachment in separated flow and increase mixing. Only recently, LSMs have been manipulated for active flow control for drag reduction [13]. As a part of an active flow control strategy, targeted manipulation of random vortical structures using a reduced order model (Dynamic Mode Decomposition with control [14]) has recently been shown useful to increase near-wall vorticity RMS [15]. More recently, Tsolovikos et al. [16] used a model predictive control scheme to develop a model based on a reduced-order representation of the flow that directs LSMs of interest closer to the wall in an optimal way via a body force-induced downwash. They highlighted the benefits of targeting fast LSMs for separation delay by enhancing momentum transfer from high- to low-momentum regions on the verge of separation, compared to a naive actuation scheme that does not account for the presence of LSMs.

The study of control of LSMs in full-scale high-fidelity DNS or experimental turbulent boundary layers can incur significant costs. Alternatively, investigating synthetic LSMs in a nominal Blasius boundary layer offers a more cost-effective approach to comprehending LSMs and their overall impact on the boundary layer under manipulation. The erratic nature of naturally occurring LSMs in turbulent boundary layers poses challenges for testing and proposing new control schemes. The laminar boundary layer (LBL) serves as a more conducive flow regime for validating certain control schemes tailored for synthetic LSMs. An idealized LSM manifests as an organized sequence of hairpin vortices, possessing a specific shape and size comparable to the boundary layer thickness [17]. While it is possible to generate LSMs in numerical simulations by applying pulsating volumetric body forces or experimentally through passive or active control methods, accomplishing this remains a challenging task.

Eitel-Amor et al. [18] found that applying short and intense pulses showed the best results for creating a single leading hairpin in a train, but secondary hairpins were created shortly after the forcing ceased, leading to a turbulent spot further downstream. Producing vortex tubes in a laminar flow can lead to the generation of hairpin vortices [19]. Recently, the work proposed in [20] suggests that a carefully tuned hyperbolic tangent (tanh) smooth distributed volumetric body force pulsating as a square wave generated a clean and stable sequence of hairpins riding a slow-moving low-speed streak if the body force pushed in the upstream direction. They also found that forcing downstream creates a fast-moving streak with similarly shaped hairpins on top.

A number of different methods have demonstrated hairpin vortex generation in an experimental setting. Acarlar and Smith [21] used passive control mechanisms in the form of hemispherical protuberances (teardrop and spherical) to generate hairpin trains from the shedding off these bodies. The same authors separately used wall-normal steady fluidic injection from a rectangular slot to generate hairpin vortex trains [22]. The unstable interaction between the low-speed streak created by the injected fluid and the incoming boundary layer yielded hairpin train formation. Impulse-based fluidic injection was used by Haidari and Smith [23] to observe the evolution of single hairpins and the subsequent auto-generation of child hairpin vortices upstream. In a related way, a synthetic jet with a round orifice was used by Jabbal and Zhong [24] to introduce hairpin vortices into a LBL. The experimental portion of the present study utilizes a similar wall-normal circular orifice shape with an unsteady blowing apparatus.

Targeting Large-Scale Motions (LSMs) selectively has been shown to significantly influence wall shear stress. When moved closer to the wall, high- or low-momentum LSMs can respectively increase or decrease wall shear stress, while enhancing mixing in both scenarios [20, 25]. Similar outcomes were observed in a fully turbulent separated boundary layer when fast-moving LSMs were brought closer to the wall, reducing the overall volume of separated flow [16, 26]. In all these studies, a body force was employed to manipulate LSMs, guiding the flow toward the wall. In practical experiments, jet-assisted surface-mounted actuators (JASMAs) [27, 28] and dielectric barrier discharge plasma actuators [29] can be used for such manipulation, instead of a hypothetical volumetric body force as simulated in [25]. Notably, the entrainment of synthetic hairpins in laminar boundary layers using JASMA has demonstrated an increase in near-wall turbulent kinetic energy (TKE) [30].

Hybrid methods represent a class of techniques designed to leverage the unique advantages of both experimental approaches and CFD for various purposes. These include noise reduction through assimilating experimental data into governing equations, uncovering unknown field quantities, enhancing resolution, and applying highly specific boundary conditions [31]. Previous studies have successfully recreated and derived field quantities by mapping PIV/PTV data onto a DNS grid as an *initial* condition. Similar approaches have been employed in modern numerical weather forecasting models, relying on sparse data measurements as initial conditions [32]. These methods enforce data compliance with governing equations, enabling the calculation of immeasurable flow quantities and resulting in reconstructed data with higher resolution and reduced noise.

Several studies have utilized unsteady PIV/PTV velocity measurements as inflow conditions at either 2D or 3D inlets, allowing the flow to evolve freely based on governing equations. Notably, a recent investigation employed 4D Particle Tracking Velocimetry (4D-PTV) data at a 3D inlet for turbulent boundary layer flow over a flat plate [33]. Techniques such as Proper Orthogonal Decomposition (POD) coupled with linear stochastic estimation (LSE) have been employed in previous studies to reconstruct realistic inflow conditions using sparse data, enabling the generation of coherent structures in large-eddy simulations [34]. The hybrid concept applied in this study is depicted schematically in Fig. 1, illustrating the spatial development of hairpin vortices.

In practice, PIV-measured data deviates from satisfying the continuity equations due to systematic errors and inherent noise. Consequently, the velocity field is generally non-divergence-free and fails to adhere to the continuity equation for incompressible flow. To address this, a divergence correction scheme is utilized, leveraging optimization techniques to find a new corrected velocity field. This corrected field aims to stay close to the true PIV data while alleviating non-zero divergence errors [35]. Expanding on this methodology, Wang et al. [36] extended the approach by

incorporating the penalized least squares regression method. This technique not only rectifies divergence errors but also smoothens noisy data, guided by an optimal smoothing parameter.

In this paper, we introduce an innovative approach to delve into the intricate physics of synthetic LSMs by combining the strengths of experiments and simulations through a hybrid physio-cyber methodology. Our physio-cyber approach utilizes stereoscopic PIV measurements at a single upstream plane to serve as the unsteady inflow boundary condition for the DNS. The idea is that the DNS would provide a smooth continuous downstream flowfield of upstream-generated experimental data. Additionally, our work aims to establish agreement between the experimentally measured flow field and its DNS counterpart. In our work, we employ a linear interpolation scheme to map raw phase-averaged PIV data onto a DNS grid at the inlet plane. To simulate the creation of synthetic hairpins, the flow spatially evolves with time-varying inflow boundary conditions based on PIV data.

The primary objective of this study is to investigate the feasibility and utility of conducting a 3D DNS utilizing 2D-PIV data as an inflow condition. The study is specifically dedicated to implementing and assessing the effectiveness of a realistic unsteady laminar inflow at the DNS inlet. The success of the investigation is gauged by comparing the freely evolving DNS field with the experimental field, thereby exposing potential mismatches and sources of errors. A central focus lies in understanding how the limited resolution of the external data source—SPIV data on a uniform rectilinear grid at discrete time intervals affects the development of hairpin vortices.

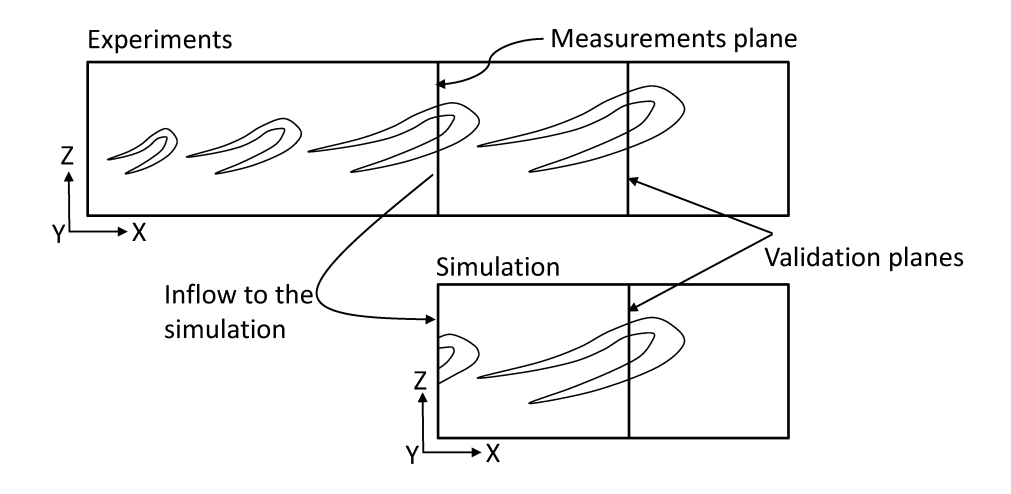


Fig. 1 Schematic representation of the hybrid physio-cyber approach.

# III. Experimental Setup

This section describes the aspects of the wind tunnel experiments used to generate planes of PIV data for data assimilation. Stereoscopic particle image velocimetry (SPIV) measurements were taken at three streamwise-normal planes to capture the artificially-generated hairpin vortices. The experiments were conducted in the low Reynolds number wind tunnel in the Center for Flow Physics and Control at Rensselaer Polytechnic Institute. The wind tunnel test section has a length of 508 mm with a square cross section with a side length of 101.6 mm. The floor of the test section was outfitted with a cutout for flush mounting a particular module for the experiments.

## A. Model Setup

This section details the aspects of the wind tunnel module used to generate synthetic vortical structures. The wind tunnel module and test domain are shown in Fig. 2. The module was printed using the stereolithography (SLA) process using Accura ABS Black (SL 7820). The vortical structures were generated using a pitched synthetic jet actuator that consisted of a piezoelectric bimorph clamped to a cavity. The synthetic jet orifice had a length of 18 mm, a width of  $h_{sj} = 1$  mm, and a pitch angle of  $\alpha = 45$  deg. The 31.2 mm diameter oscillating bimorph membrane resonated in a 3.0 mm thick circular cavity of diameter 36.0 mm. The cavity extended 23.0 mm to the surface where vortical structures issued into the crossflow. The actuator was driven by a sine wave signal with a frequency of f = 1.1 kHz, a frequency

that was slightly off-resonance of the piezoelectric bimorph. The amplitude was adjusted such that the peak velocity measured by a hot wire probe at the jet exit plane was consistent with a blowing ratio of  $C_b = 0.5$ .

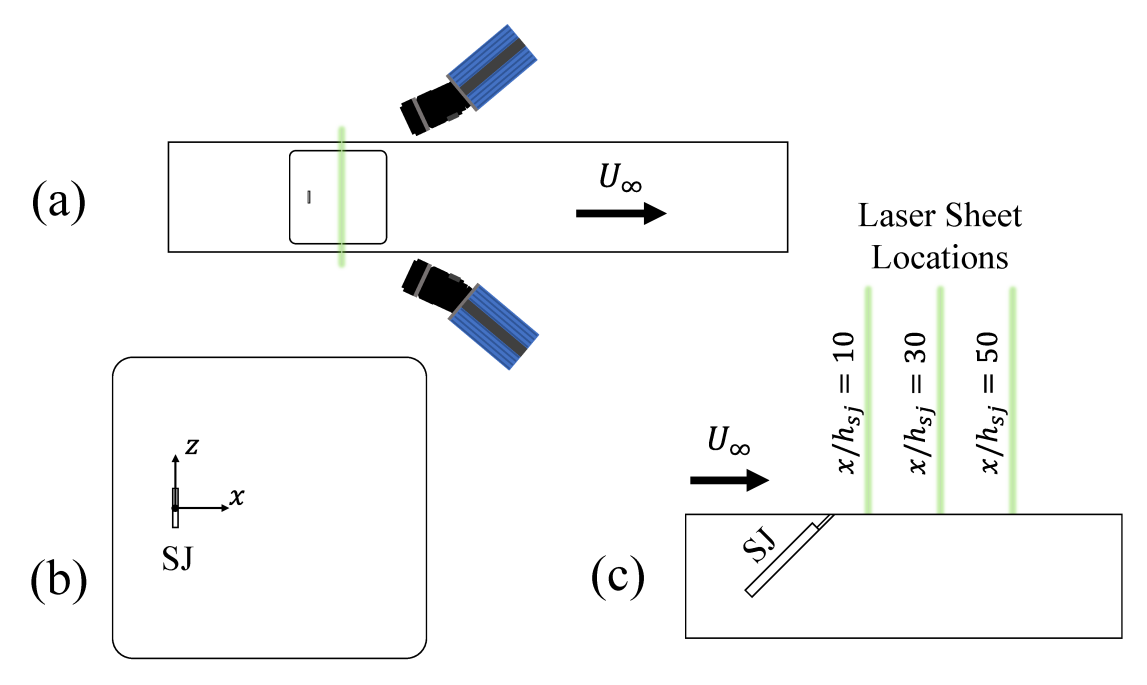


Fig. 2 Wind tunnel SPIV setup (a), measurement planes (b), and section view of the pitched synthetic jet (c).

At the location of the synthetic jet center, the incoming flow had a laminar boundary layer with a thickness of  $\delta = 3.0$  mm, a displacement thickness of  $\delta^* = 1.0$  mm, a momentum thickness of  $\theta = 0.4$  mm, and a shape factor of H = 2.71. The baseline boundary layer was compared against the Blasius profile to ensure that the boundary layer is laminar.

## **B.** Stereoscopic Particle Image Velocimetry

Details about the SPIV setup and acquisition are provided in this section. Phase-locked SPIV measurements were collected at 72 phases regularly-spaced during the synthetic jet actuation cycle. The planes were acquired at three streamwise-normal planes at  $x/h_{sj} = 10$ , 30, and 50. The location of  $x/h_{sj} = 0$  represents the center of the jet orifice. The beam from a New Wave 120 mJ Nd:YAG double-pulsed laser was focused using an adjustable focal lens (focal length of 500 to 3000 mm) and fanned into a sheet of thickness ≈ 1 mm using a cylindrical lens with -20 mm radius. The laser sheet illuminated water-glycol mixture tracer particles with mean diameter  $O(1 \mu m)$  that were seeded and dispersed upstream of the tunnel for uniform coverage of the flow domain. Two 2 Megapixel LaVision Imager Pro X CCD cameras with 100 mm Tokina lenses were used to capture 250 image pairs per case at each plane, each with a size of 50.7 mm × 28.6 mm. The data acquisition domain was sufficiently small enough that effects from the boundary layers on the top and side walls of the wind tunnel were not present. Data were collected using the DaVis 8.4.0 software and a programmable timing unit to synchronize the laser firing and camera acquisition to the jet blowing. The images were processed using a stereoscopic double-exposure cross-correlation algorithm to yield vector fields with a resolution of 2.97 vectors/mm in both in-plane directions. Interrogation windows of decreasing size were used: 48 pixels × 48 pixels for the first pass and 24 pixels  $\times$  24 pixels for the second two passes, each with 50% overlap. The vector fields were corrected to minimize the disparity vector between the laser sheet and the camera focal planes using a stereoscopic self-calibration algorithm. Each phase of the data was acquired 12.6  $\mu$ s apart, and 250 image pairs were ensemble-averaged to generate the phase-locked images used in the hybrid data assimilation method.

# **IV. PIV Data Processing**

This section delineates the essential processing steps undertaken to transform raw PIV data into a format suitable for serving as the inflow boundary condition for DNS. It involves a two-fold approach, wherein we first pre-process the data employing a divergence correction scheme to satisfy the continuity quation. We follow this by a straightforward linear

interpolation technique to map the coarse PIV data onto the DNS grid.

#### A. Divergence Correction

The velocity data obtained through the planar SPIV technique are susceptible to systematic errors arising from inherent experimental uncertainties. These errors can lead to non-zero divergence of the velocity field,  $\nabla \cdot \mathbf{U} \neq 0$ , where  $\mathbf{U}$  is the velocity vector. Such discrepancies compromise the satisfaction of the continuity equation. To remedy this, we implement technique proposed by de Silva et al. [35]. This method uses an optimization approach to compute a new vector field which adheres to the continuity equation for incompressible flow, i.e.  $\nabla \cdot \mathbf{U}_{corr} = 0$ , where  $\mathbf{U}_{corr}$  is the corrected velocity. This formulation ensures that the corrected velocity field remains as close as possible to the measured data, mitigating the impact of systematic errors and enhancing the fidelity of the corrected data.

The optimization problem is formulated to ensure that the corrected velocity field,  $U_{corr}$ , closely aligns with the ground truth, represented by the measured PIV data. This alignment is achieved by minimizing the  $L_2$  norm of the difference between the two velocity fields, subject to the linear constraint of satisfying the continuity equation. The objective function for the optimization problem is defined as the minimization of the  $L_2$  norm, expressed as:

$$\min_{\mathbf{U}_{\text{corr}}} \| \mathbf{U} - \mathbf{U}_{\text{corr}} \|_{2}^{2}$$

$$s.t.\nabla \cdot \mathbf{U}_{\text{corr}} = 0$$
(1)

Here, the divergence of the velocity field is numerically approximated using a second-order finite-difference scheme for all the interior points and first-order one-sided difference scheme is used for exterior boundary data points. To compute the gradient at each spatial location, the spacing in the wall-normal ( $\Delta y$ ) and spanwise ( $\Delta z$ ) directions matches the uniform grid spacing of the PIV resolution in those respective directions—specifically,  $0.1078\delta_{in}$  in this case. Simultaneously, the spacing in the streamwise ( $\Delta x$ ) direction is set equal to non-dimensional PIV data acquisition timestep  $dt_{PIV}$ .

The linear constraint in Eq. (1) can be expressed as a set of linear equation at each spatial location.  $\nabla \cdot \mathbf{U}_{\text{corr}} = 0$  can be written as  $\mathbf{A}x = \mathbf{b}$ , where  $\mathbf{A}$  is the sparse matrix of coefficients obtained from a finite-difference scheme as per Eq. (2), x is the reshaped column velocity vector and  $\mathbf{b}$  is equal to the zero column vector in this case. In this study, a total of  $n = n_x \times n_y \times n_z = 72 \times 40 \times 146$  spatial points are used. Here,  $n_x = 72$  corresponds to the number of phases available to be used as inflow boundary condition with temporal spacing of  $dt_{PIV}$  between each phase. Each plane is measured at some distance downstream of the synthetic jet as mentioned in Subsection III.B.

The sparse matrix **A** takes a specific form given by the following expression for a chosen finite-difference scheme [36]:

$$\mathbf{A} = \left[ \frac{1}{\Delta x} \mathbf{I}_{n_z} \otimes \mathbf{I}_{n_y} \otimes \mathbf{D}_{n_x}, \frac{1}{\Delta y} \mathbf{I}_{n_z} \otimes \mathbf{D}_{n_y} \otimes \mathbf{I}_{n_x}, \frac{1}{\Delta z} \mathbf{D}_{n_x} \otimes \mathbf{I}_{n_y} \otimes \mathbf{I}_{n_x} \right]$$
(2)

Where  $I_m$  is identity matrix of size  $m = n_x$ ,  $n_y$  or  $n_z$ , and  $D_m$  takes the following form

$$\mathbf{D}_{m} = \begin{bmatrix} -1 & 1 & & & \\ -1/2 & 0 & 1/2 & & \\ & -1/2 & 0 & 1/2 & & \\ & & & \ddots & & \\ & & & -1 & 1 & \\ & & & & \ddots & \\ & & & & -1 & 1 & \\ \end{bmatrix}$$
(3)

Prior to solving the optimization problem at hand, the velocity data from PIV is normalized by  $U_{\infty}$ , while the spatial data points are normalized by the hydrodynamic boundary layer thickness  $\delta_{\rm in}$ . The optimization problem is tackled using the CVXPY optimization toolkit [37]. As demonstrated in Fig. 3, the implemented divergence correction scheme significantly improves the quality of the PIV data by effectively eliminating errors associated with non-zero divergence. In Fig. 3a and 3b, a slice of the divergence field for the PIV dataset is displayed before and after the optimization, respectively. It is crucial to note the scales in these plots, as the optimization has reduced the divergence to the order of  $10^{-14}$ . Fig. 3c illustrates the absolute change in the streamwise velocity component resulting from the divergence correction.

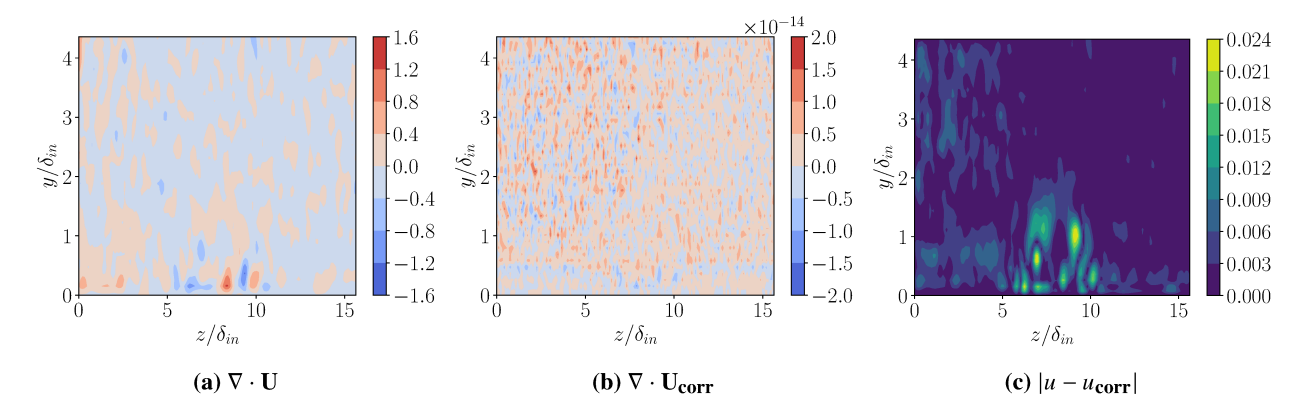


Fig. 3 A slice of PIV dataset showing divergence field (a) before and (b) after the optimization, (c) absolute error in streamwise velocity

# **B. Spatial and Temporal Interpolation**

To prepare for the unsteady velocity inlet to the DNS inflow boundary condition, the DNS inlet requires velocity information at every DNS grid point for a given timestep. As the PIV data are obtained on a uniform rectilinear grid, a spatial interpolation scheme is essential to remap the data onto the DNS grid. Additionally, a temporal interpolation scheme is required to provide data at every DNS substep. It is to be noted that the divergence correction scheme outlined in previous section is not applied at every DNS substep. Fig. 4 shows a conceptual general approach implementing the hybrid algorithm where  $\mathbf{u}_t^{\text{DNS}}$  at every DNS timestep is computed using available velocity data at discrete PIV timesteps using Eq. (4) and (5). PIV data are obtained for a single actuation cycle, consisting of 72 phases. Consequently, to construct a sequence of hairpins, the PIV data are periodically cycled through the computational domain at the inlet.

$$\begin{pmatrix} u \\ v \\ w \end{pmatrix}^{PIV} \xrightarrow{dt_{PIV}} \begin{pmatrix} u \\ v \\ w \end{pmatrix}^{PIV} \xrightarrow{dt_{PIV}} \begin{pmatrix} u \\ v \\ w \end{pmatrix}^{PIV} \dots$$

$$\downarrow \qquad \qquad \downarrow \qquad \downarrow \qquad \qquad \downarrow \qquad$$

Fig. 4 Conceptual diagram of the hybrid algorithm

First, at the inlet for each DNS timestep, the PIV velocity data are interpolated using a linear temporal interpolation scheme as follows:

$$\mathbf{u}_{t}^{\text{PIV}} = \frac{\mathbf{u}_{\lfloor t \rfloor}^{\text{PIV}} \{ (\lfloor t \rfloor + dt_{\text{PIV}}) - t \} + \mathbf{u}_{\lfloor t \rfloor + dt_{\text{PIV}}}^{\text{PIV}} \{ t - \lfloor t \rfloor \}}{dt_{\text{PIV}}}$$
(4)

where,  $\lfloor \cdot \rfloor$  is the floor function applied to the non-dimensional time t,  $\mathbf{u}_t^{\text{PIV}}$  is the PIV data interpolated at time t.  $\mathbf{u}_t^{\text{PIV}}$  is then used to map PIV data onto a DNS grid at the inflow plane (x=0) using the bi-linear spatial interpolation method. Since the x coordinate location is fixed at the inlet of the DNS, Eq. 5 can be used at every (x,y,z) location of the DNS inlet grid to compute  $\mathbf{u}_t^{\text{DNS}}(y,z)$  at any given coordinate (y,z) bounded by the coordinates from PIV grid such that  $y_2 \leq y \leq y_1$  and  $z_2 \leq z \leq z_1$ . Given 4 PIV coordinates  $Q_{11} = (y_1,z_1)$ ,  $Q_{12} = (y_1,z_2)$ ,  $Q_{22} = (y_2,z_2)$ , and  $Q_{21} = (y_2,z_1)$ , bi-linear interpolation can be written as,

$$\mathbf{u}_{t}^{\text{DNS}}(y,z) = \frac{1}{(y_{2} - y_{1})(z_{2} - z_{1})} \begin{bmatrix} y_{2} - y & y - y_{1} \end{bmatrix} \begin{bmatrix} \mathbf{u}_{t}^{\text{PIV}}(Q_{11}) & \mathbf{u}_{t}^{\text{PIV}}(Q_{12}) \\ \mathbf{u}_{t}^{\text{PIV}}(Q_{21}) & \mathbf{u}_{t}^{\text{DNS}}(Q_{22}) \end{bmatrix} \begin{bmatrix} z_{2} - z \\ z - z_{1} \end{bmatrix}$$
(5)

Given the limitations in spatial resolution of the PIV system and due to laser reflections, very few points are available near the wall to capture the near-wall velocity gradient within the boundary layer. The resolution of the PIV grid was  $n_y = 40$  in the wall-normal direction covering  $y = 0.13\delta_{\rm in}$  to  $4.5\delta_{\rm in}$  and  $n_z = 146$  covering spanwise extent of z = 0 to  $16\delta_{\rm in}$ . The near wall region, which was not resolved in the present PIV measurements, is shown as  $y_{\rm offset}$  in Fig. 7. It was observed that a linear velocity profile is a good enough first-order approximation to a Blasius velocity profile very close to the wall. Hence, to preserve the no-slip boundary condition ( $U_{y=0} = 0$ ) and for simplicity, a linear blending scheme is employed for this region (y = 0 to  $y_{\rm offset}$ ) until the first PIV data are available for all three components (u, v, and w) as illustrated in Fig. 5.

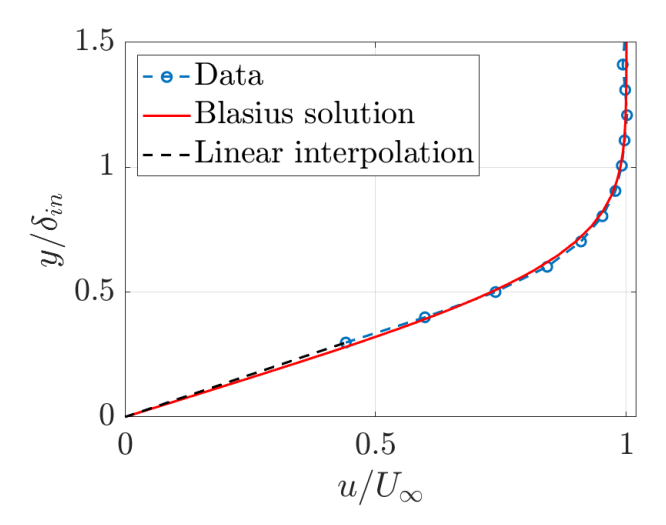


Fig. 5 Comparison of the experimental boundary layer (blue circles with dotted line), Blasius boundary layer solution (red line), and linear interpolation to satisfy the no-slip boundary condition (black dotted line).

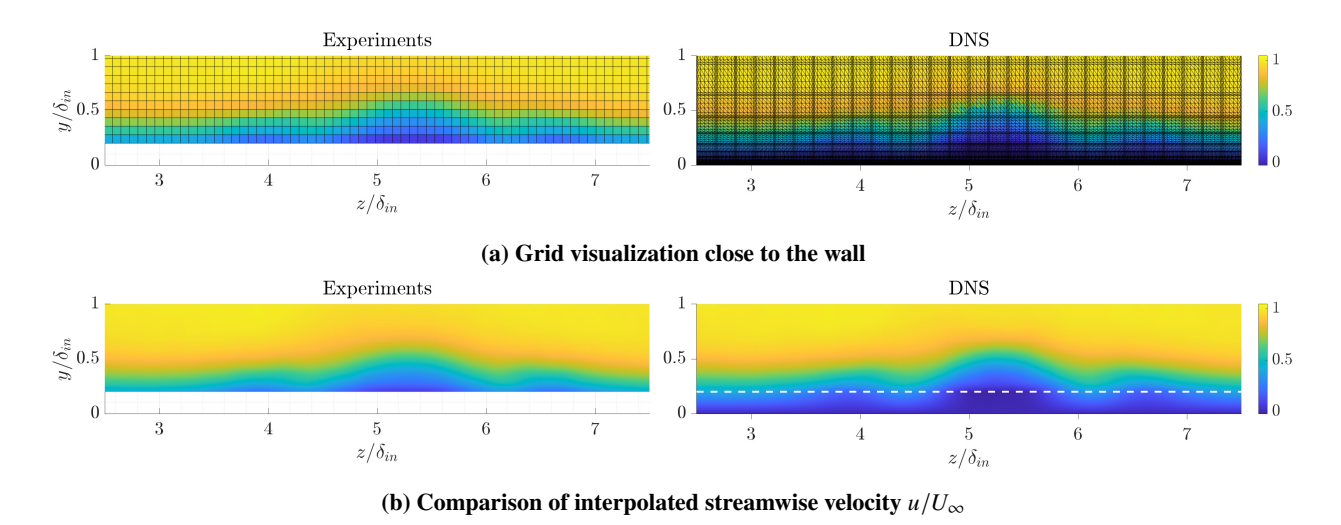


Fig. 6 Representation of the interpolated PIV grid data on a DNS grid at the inlet of a DNS at one particular instant in time

The representation of the PIV and DNS grids near the wall is illustrated in Fig. 6, along with a comparison of the

interpolated streamwise velocity component u. The area below the white dashed line in Fig. 6b corresponds to the linear wall blending approach, where PIV data is not available due to laser reflection.

# V. Numerical Setup

This section elaborates on the computational setup employed for the hybrid simulation, integrating PIV data as the inflow boundary condition. The pre-processing and interpolation steps, outlined in previous sections, are fundamental to this setup. Within this section, we provide comprehensive details regarding the DNS domain, the flow solver, boundary conditions, and crucial flow parameters.

# A. Computational Domain and Boundary Condition

This study employs a high-fidelity DNS solver for the nominally zero-pressure gradient laminar flow past a flat plate. The incompressible Navier-Stokes and continuity equations

$$\frac{\partial \mathbf{U}}{\partial t} + \mathbf{U} \cdot \nabla \mathbf{U} = -\nabla P + \frac{1}{Re_{\delta_{\text{in}}}} \Delta \mathbf{U} + \mathbf{F}$$
 (6)

$$\nabla \cdot \mathbf{U} = 0 \tag{7}$$

are non-dimensionalized by the free-stream velocity,  $U_{\infty}$ , and the 99% boundary layer thickness,  $\delta_{\rm in}$ , at the inlet of the DNS. The reference values of these parameters are listed in Table 1. The governing Eqs. 6 and 7 are solved using a high-order spectral element solver Nek5000 [38]. The position  $\mathbf{X} = [x, y, z]$  and velocity  $\mathbf{U} = [u, v, w]$  vectors consist of their streamwise, wall-normal, and spanwise components, respectively. During the experiments, the undisturbed boundary layer thickness at the location 30 mm downstream of the synthetic jet during the experiments was  $\delta_{\rm in} = 3.1$  mm, and free stream velocity was  $U_{\infty} = 10.5$  m/s. The Reynolds number based on  $\delta_{\rm in}$  is  $Re_{\delta_{\rm in}} = 2072$ .

Fig. 7 shows the relative position of the inlet section with respect to the jet orifice used to generate synthetic hairpins. The DNS domain is truncated to only use a portion of the full experimental domain. The dimensions of the computational setup are as follows: the streamwise length of the domain is  $L_x = 20\delta_{\rm in}$ , the height is  $L_y = 4\delta_{\rm in}$ , and the spanwise extent is  $L_z = 7.5\delta_{\rm in}$ . The domain is decomposed into  $N_x = 100$ ,  $N_y = 15$ , and  $N_z = 24$  spectral elements in streamwise, wall-normal, and spanwise directions, respectively. Each spectral element represents the velocity and pressure field in the form of a 7th-order Gauss-Lobatto-Legendre polynomial. As depicted in Fig. 6a, the DNS grid is stretched in wall-normal direction facilitated by a hyperbolic tangent (tanh) function.

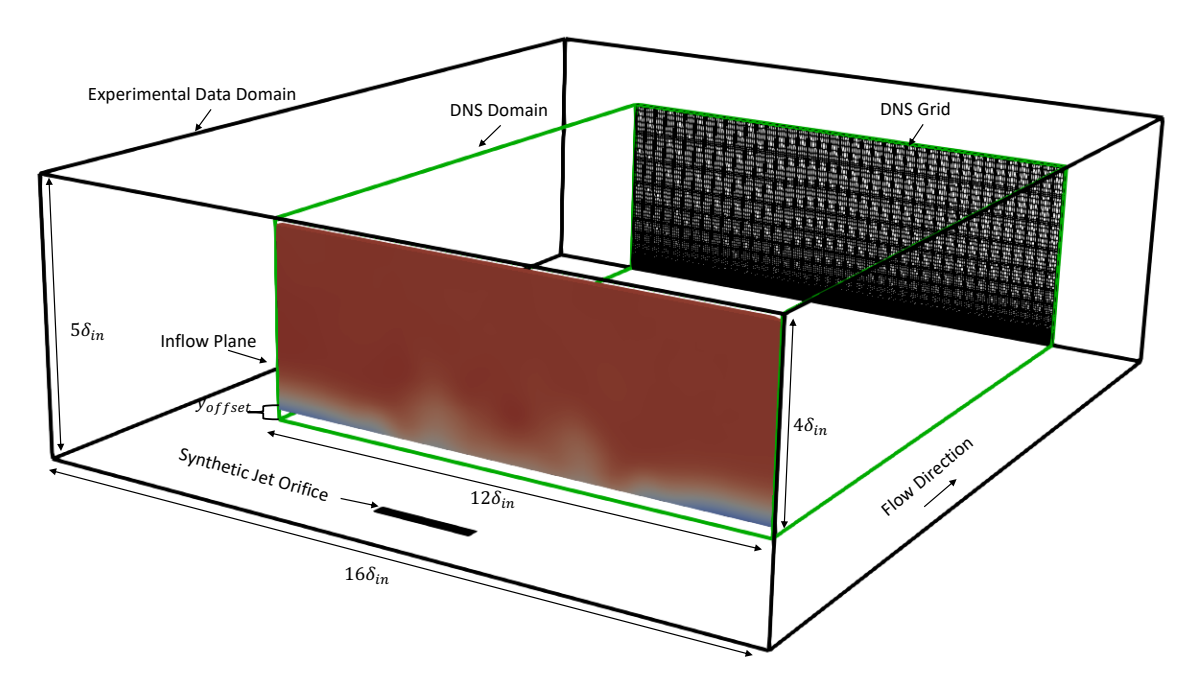


Fig. 7 Numerical setup

The rest of the domain boundary conditions are as follows: no-slip boundary condition at the wall, periodic boundary conditions in the spanwise direction, and an outflow boundary condition  $([-PI + \nu(\nabla \mathbf{U})] \cdot \mathbf{n} = 0)$  at the top and at the outlet are applied where  $\mathbf{n}$  is a normal outward vector.

#### **B. Flow Parameters**

The dimensional and non-dimensional parameters are listed in Table 1. PIV measurements were conducted at three distinct downstream locations: 10 mm, 30 mm, and 50 mm from the synthetic jet orifice. Specifically, in the Table 1, the Reynolds number associated with the inlet hydrodynamic boundary layer thickness is determined for the location 30 mm downstream of the synthetic jet.

The timestep for DNS is set at  $dt_{\rm DNS} = \frac{0.005 \, \delta_{\rm in}}{U_{\infty}}$ . PIV data were acquired with a time interval of  $dt_{\rm phase} = 12.65 \, \mu \rm s$ ,  $U_{\infty} = 10.5$  m/s, and  $\delta_{\rm in} = 3.1$  mm, resulting in a non-dimensional timestep for PIV,  $dt_{\rm PIV} = \frac{dt_{\rm phase} U_{\infty}}{\delta_{\rm in}} = 0.0425$ . The total number of temporal interpolation steps required between each PIV phase, denoted as  $N_{\rm DNS}$ , is a function of the non-dimensional DNS and PIV timesteps, as illustrated in Fig. 4.

Parameter	Exp.	DNS
$Re_{\delta_{in}}$	2072	2072
$U_{\infty}$	$10.5 \ m/s$	1
$\delta_{ m in}$	$3.1 \ mm$	1
ν	$15.71 \ mm^2/s$	1/2072
$dt_{\rm phase}$	12.65 $\mu s$	0.043

Table 1 Exp. and DNS flow parameters

## VI. Results

To assess the efficacy of the hybrid physio-cyber approach, two separate simulation sets were conducted for validation. First, unsteady velocity data from independent DNS runs were employed to confirm that by generating disturbances in DNS and treating them as PIV data, the expected DNS results downstream could still be recovered. Following this, actual unsteady PIV data were utilized, and the results were cross-validated against volumetric PIV measurements.

#### A. Inflow Using Unsteady DNS Data

Following a methodology akin to experiments, hairpins within the LBL were generated using the approach elucidated by Jariwala et al. [20]. This technique employs a hyperbolic tangent (tanh) distributed body force to create synthetic hairpins. The frequency of body force actuation was temporally modulated by a square wave and other parameters were systematically adjusted to produce a sequence of hairpins tailored for Reynolds numbers comparable to those investigated in the experiments conducted for this study.

Fig. 8 shows hairpins generated by the body force (dark gray contour) actuation in a laminar boundary layer for  $Re_{\delta_{\rm in}}=2000$  at the inlet of the computational domain. The length of computational domain in streamwise, wall-normal and spanwise direction is  $L_x=25\delta_{\rm in},\,L_y=5\delta_{\rm in},\,$  and  $L_z=5\delta_{\rm in},\,$  respectively. The hairpins are shown as Q-criterion iso-surfaces colored by the streamwise vorticity  $\omega_x$ . The wall is colored by the streamwise velocity gradient in wall-normal direction,  $\partial u/\partial y$ .

The location of the measurement plane  $(x = 10\delta_{\rm in})$  from the inlet (x = 0) is deliberately chosen to strike a balance: it is neither too close to the body force to avoid sharp gradients nor too far away, ensuring that the hairpins remain discernible without dissipating away. The measurement plane consists of a collocation of points with a uniform distribution in the wall-normal and spanwise directions. The number of points in each direction and the acquisition frequency are varied to assess the effects of the physio-cyber approach. The data were acquired for one non-dimensional time unit, consisting of  $N_{\rm phase}$  phases.

To provide an initial assessment of the effectiveness of the inflow boundary condition, Fig. 9 offers a comparison between hairpins generated through body force actuation as in Fig. 8 and those produced using inflow boundary conditions derived from velocity measurements at the measurement plane. In this comparison, a total of  $n_y \times n_z = 47$ 

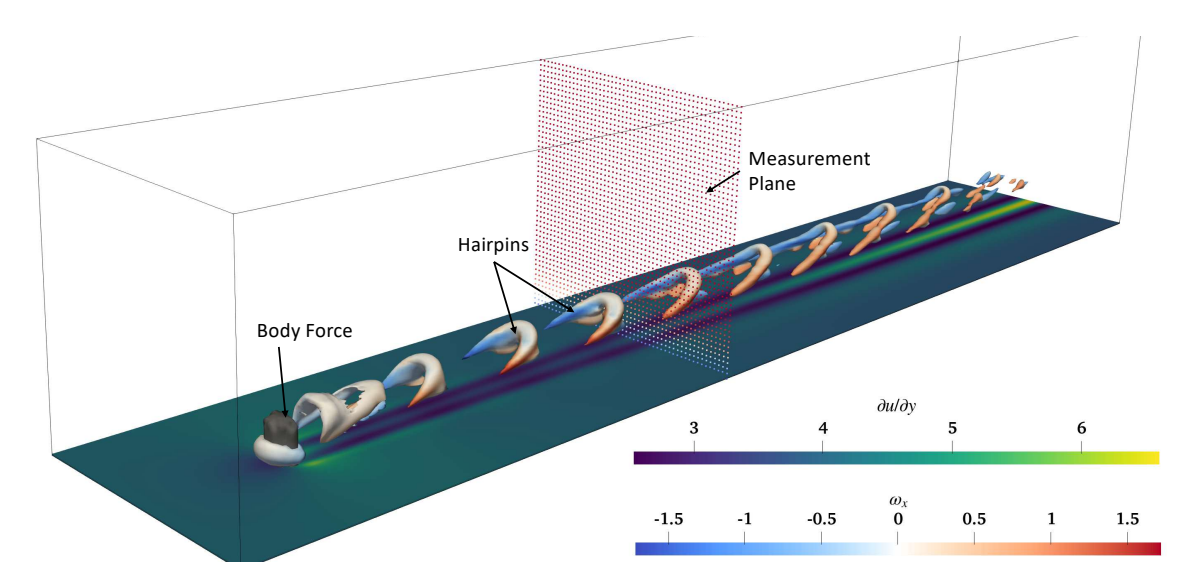


Fig. 8 Generation of synthetic hairpins in a DNS via body force actuation

points  $\times$ 47 points were employed to measure velocity at every  $4dt_{\rm DNS}$  timestep, resulting in a total of  $N_{\rm phase} = 51$  phases for one non-dimensional time unit. These parameters were deliberately selected to align with the setup parameters of the PIV measurements for a more meaningful comparison.

The initial hairpin structures, as visualized through Q-criterion iso-surfaces, exhibit an identical appearance. However, as we look further downstream, the iso-surfaces do not align precisely. Despite the acquisition frequency potentially being sufficient to resolve temporal scales, the extraction of DNS data onto a lower-resolution measurement plane results in spatially under-resolved velocity information. To validate how well the inflow boundary condition performed, various measurement grids of different resolutions were employed to acquire a more comprehensive understanding of the results.

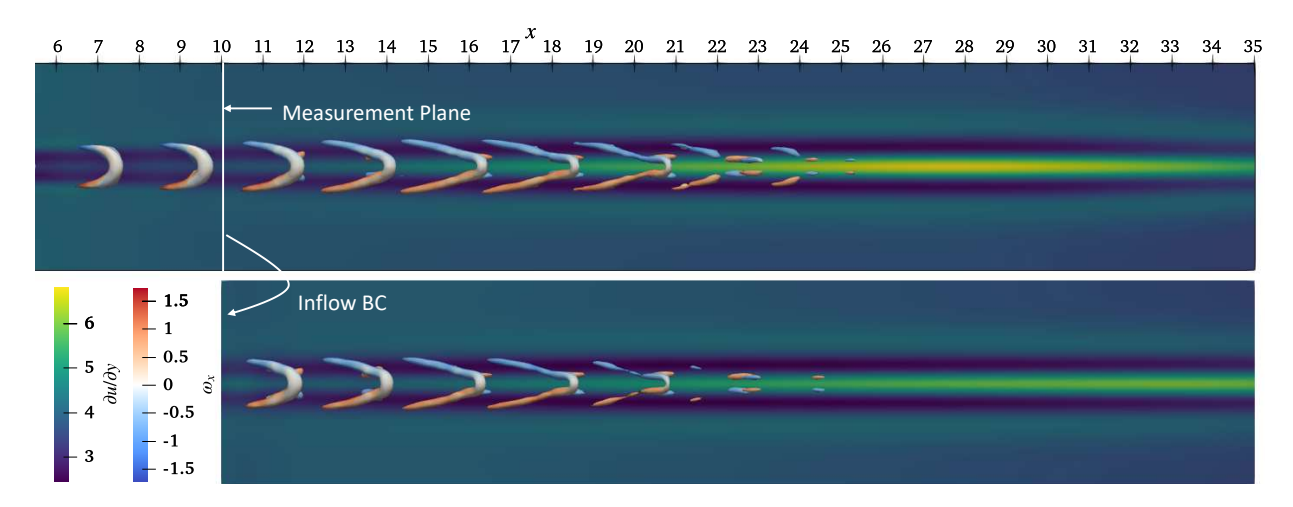


Fig. 9 Comparison of flow fields (top down view): Top - DNS using body forces, Bottom - DNS using inflow BC

# 1. Effect on the wall shear stress

To evaluate the hybrid simulation's performance, we examine the normalized wall-shear stress ( $C_f = \tau_w/\rho U_\infty^2$ ) along the centerline of the bottom wall. Employing four different combinations of measurement plane grid resolution and acquisition frequency allows us to ovserve their distinct effects. Initially, within the region  $x = 10\delta_{\rm in} - 20\delta_{\rm in}$ , the friction coefficient closely aligns with the reference simulation, as illustrated in Fig. 10. However, beyond  $20\delta_{\rm in}$ , the  $C_f$ 

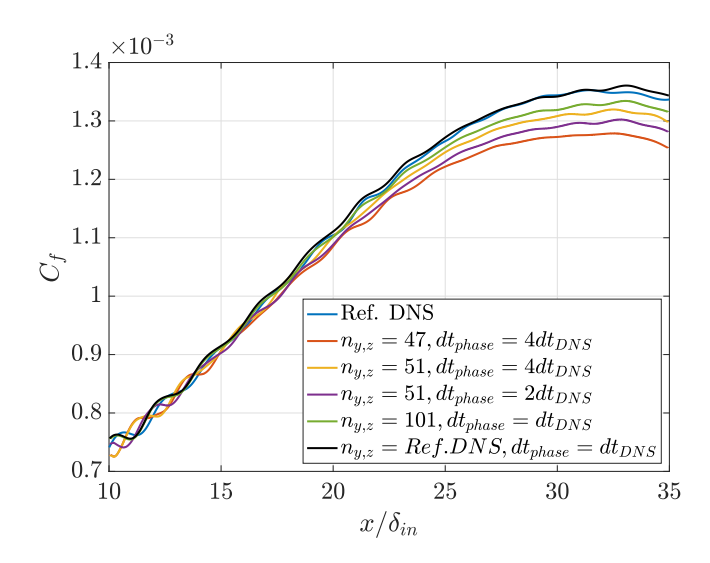


Fig. 10 Comparison of friction coefficient  $(C_f)$  for various measurement plane grid resolution and acquisition frequency along the centerline of the bottom wall

values diverge. This divergence stems from each case capturing varying levels of information, resulting in a loss of fidelity in the measured data and a departure from the true state. It's important to note that the results presented here reflect the quasi-steady-state of the hairpin evolution.

The blue curve serves as a reference for the DNS simulation, wherein hairpins are generated using body force. However, the case with a grid resolution of  $n_{y,z}=47$  and  $dt_{\rm phase}=0.02$ , aligning with the PIV parameters, effectively captures and reproduces the flowfield (red curve). While it demonstrates promising performance, there is room for potential refinements to enhance accuracy. The most favorable outcomes are observed for the grid resolution, which is  $2\times$  finer than PIV, and  $dt_{\rm phase}=dt_{\rm DNS}$ , depicted by the green curve. To further analyze the performance, an additional simulation with the measurement plane grid exactly matching the DNS grid and data acquisition frequency aligning with the DNS timestep was conducted. As indicated by the black line, coinciding well with the reference blue curve, it demonstrates the agreement and feasibility of the hybrid inflow boundary condition.

# **B. Inflow Using Unsteady PIV Data**

As illustrated in Fig. 2, PIV data were obtained at three specific locations: x = 10 mm, x = 30 mm, and x = 50 mm downstream of the synthetic jet. Subsequently, Fig. 11 showcases Q-criterion iso-surfaces colored by the streamwise vorticity for the resulting flow downstream of each of these planes when employed as inflow boundary conditions in the hybrid physio-cyber simulation. The structures (white-gray contours) observed near the wall in the inlet section for each case are non-physical artifacts arising from the interpolation near the wall to maintain the no-slip boundary condition. However, these structures rapidly dissipate within the simulation.

The orange rectangular box outlined in the upper portion of Fig. 11 represents the region within the experimental domain where phase-locked volumetric SPIV data were measured. This data is qualitatively compared with iso-surfaces in the DNS results, as presented in Section VI.B.2.

Clearly, the flow generated using the inflow boundary condition derived from the plane located at x = 10 mm (11a) does not manifest distinct evidence of hairpin structures. The close proximity to the synthetic jet results in high-speed flow emanating from the jet orifice, leading to unresolved velocity gradients with the available coarse PIV measurements. Moreover, these unsteady velocity components are linearly interpolated to the wall to preserve the no-slip boundary condition. This linear approximation to the nonlinear development of the hairpin may contribute to the development of an unstable flow.

Proceeding further, Figures 11b and 11c reveal a more stable flow development when utilizing the inflow boundary conditions derived from planes located at x = 30 mm and x = 50 mm, respectively: these planes produce more satisfactory results. Henceforth, all flow visualizations are presented for these two planes. Given the availability of subsequent planar data at and beyond the x = 30 mm plane, measurements at the 50 mm plane are employed to validate the flow generated using the x = 30 mm plane.

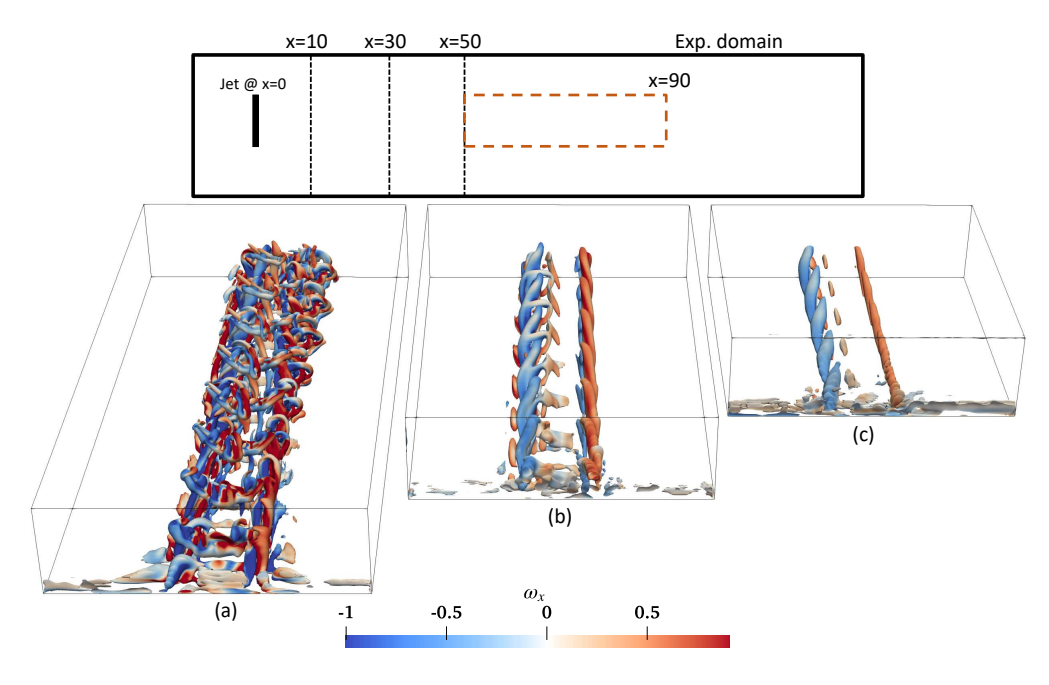


Fig. 11 Upper Figure: Schematic representation of the experimental setup. Lower Figure: Flow visualization depicting three different inflow boundary conditions derived from planes located at (a) x = 10 mm, (b) x = 30 mm, and (c) x = 50 mm.

## 1. Volume averaged velocity comparison

Considering the finite thickness of the laser sheet, as seen in Figure 2, employed for PIV measurements, there is a susceptibility to averaging along the thickness of the laser. To ensure a faithful comparison between DNS results and PIV data at the validation plane x = 50 mm, specifically for the flow generated using inflow data derived from the x = 30 mm plane, the volume data centered at  $x = 6.4 \pm 0.15\delta_{in}$  within the DNS domain is subjected to mild streamwise averaging.

The bar symbol ( $\bar{\cdot}$ ) indicates a volume-averaged quantity in the streamwise direction. In Fig. 13, all three volume-averaged velocities are compared with the corresponding values obtained from PIV measurements. Notably, the hybrid simulation demonstrates an accurate capture of flow field details, compensating for the spatial resolution limitations in PIV measurements. This is particularly evident in the upscale representation of data, providing finer details.

#### 2. Volumetric SPIV and DNS data

Phase-locked volumetric SPIV measurements were used for a visual comparison of the hairpin vortices generated through the physio-cyber approach. Phase-locked volumetric PIV data were acquired in the experimental setup spanning from x = 50 mm to x = 90 mm, as indicated by the dashed orange line in Fig. 11. For the physio-cyber simulation, data at x = 50 mm were utilized to generate the inflow boundary condition. This particular run yielded the most accurate representation of the flow field, particularly in terms of developing hairpin vorticity magnitude.

Three distinct contour plots of Q-criterion, color-coded by streamwise vorticity, are presented in Fig. 12: (a) Q-criterion computed directly from PIV measurements, (b) DNS data mapped onto a PIV grid, and (c) the original DNS grid data. The hairpin structures in all three cases closely resemble each other. Notably, (b) and (c) lack the background very near-wall structures (noise) visible in the PIV data, while simultaneously capturing finer higher altitude hairpin structures around the legs.

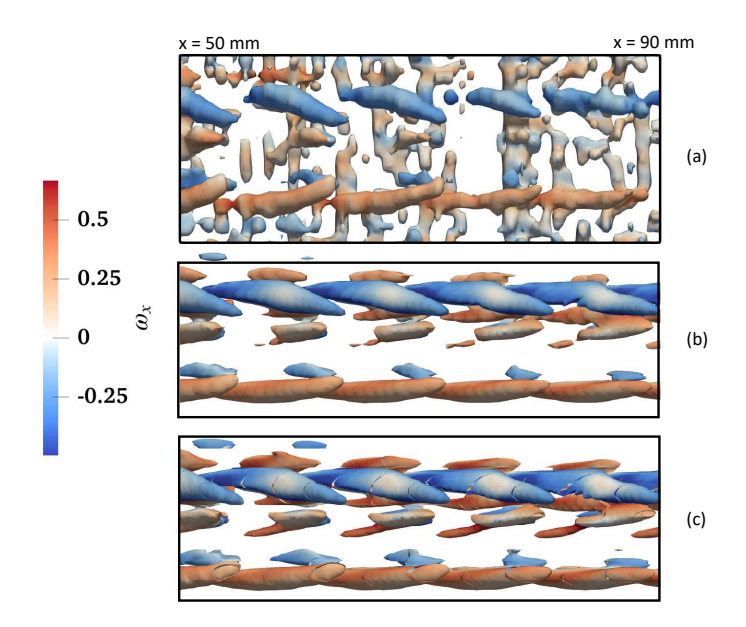


Fig. 12 Q-criterion iso-surface comparison for three different grid resolution: (a) PIV data (b) DNS data mapped onto PIV grid (c) DNS data on the full DNS grid

## VII. Conclusion and Future Work

The current study has presented a proof-of-concept approach for using an experimental unsteady inlet boundary condition for the DNS solver to examine complex unsteady flows. The results outlined herein should be considered preliminary, as they serve to explore the potential of the proposed methodology and highlight associated difficulties. In this particular case, PIV experiments were conducted to acquire unsteady velocity data at discrete pjase-locked time intervals. These experiments utilized synthetic jet actuation to generate a sequence of hairpin vortex trains over a flat plate.

To compensate for the spatial resolution limitations of the PIV setup, a divergence correction scheme was employed to address minor non-physicalities that arose. Additionally, laser reflection prevented the capture of velocity information near the wall, necessitating the implementation of a wall blending scheme to maintain the no-slip boundary condition for the DNS. Linear temporal interpolation and bi-linear spatial interpolation were utilized to map the data onto a DNS grid for the inflow boundary condition.

The limitations of the approach became apparent through a benchmark problem using inflow data obtained from a separate DNS with hairpin vortices. Examining the downstream flow replication revealed challenges in achieving full fidelity. Insights into these limitations were gained by analyzing the development of wall-shear stress in the domain after incorporating inflow boundary conditions. It was observed that the accuracy of the flow is notably influenced by the characteristics of the measurement grid, such as PIV, and the use of a simplistic linear interpolation scheme introduces additional sources of error.

Finally, inflow data derived from three different PIV measurements were tested. The results demonstrate satisfactory agreement between PIV and hybrid DNS. As evident in Fig. 11, the PIV grid resolution was seemingly insufficient for the x=10 mm data to be used as an inflow condition due to sharp velocity gradients on that plane. The volumetric flow visualization reveals the large-scale similarity between experiments and physio-cyber hybrid data when x=50 mm were used and the ability to identify equivalent structures in both datasets, which are highly encouraging outcomes of these results.

In light of the insights gained from this data, future studies will aim to enhance the accuracy of the results by employing higher-order temporal and spatial interpolation schemes. Additionally, a more in-depth analysis will be conducted to track the streamwise evolution of flow quantities. A spatial low-pass convolution filter may be applied to the DNS results in an attempt to create a more realistic analogy for the experimental procedure, which is practically limited in resolution.

# VIII. Acknowledgments

This work was funded by the National Science Foundation under award numbers 2129494 (monitored by Dr. Ron Joslin) and 2052811 (monitored by Dr. Eva Kanso). The authors acknowledge the Texas Advanced Computing Center (TACC) at the University of Texas at Austin for providing high-performance computing resources that have contributed to the results of this work. The authors would also like to thank Jasmine Narine for help with model design for the wind tunnel experiments and Paul Remneff and Lilly Mertzlufft for help with experimental data acquisition.

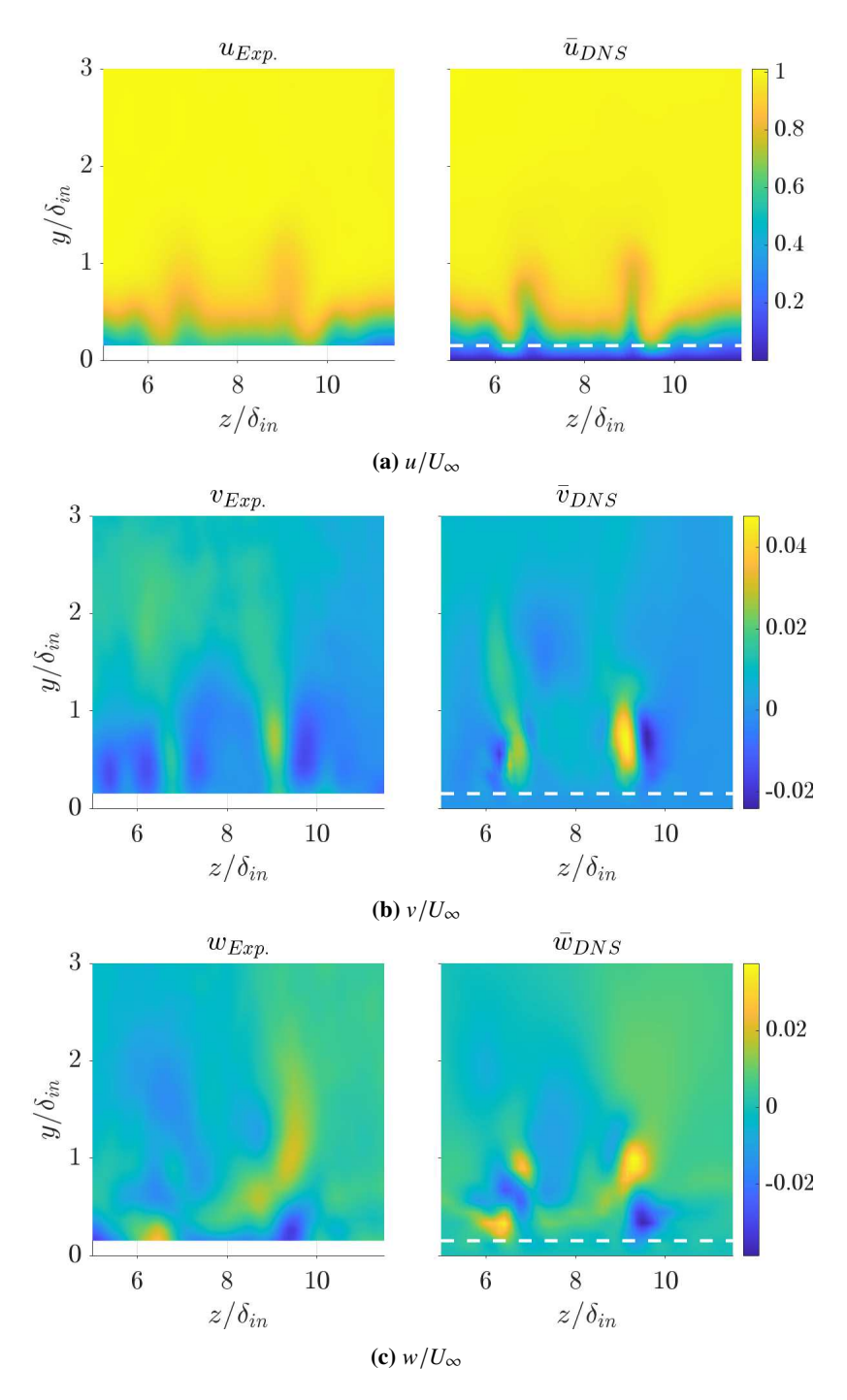


Fig. 13 Comparison of volume averaged streamwise (a), wall-normal (b), and spanwise (c) components of the velocity at the x = 50 mm

## References

- [1] Robinson, S. K., "Coherent motions in the turbulent boundary layer," *Annu. Rev. Fluid Mech*, Vol. 23, No. 1, 1991. https://doi.org/10.1146/annurev.fl.23.010191.003125.
- [2] Liu, Z., Adrian, R. J., and Hanratty, T. J., "Large-scale modes of turbulent channel flow: transport and structure,", 2001. https://doi.org/10.1017/S0022112001005808.
- [3] Kim, K. C., and Adrian, R. J., "Very large-scale motion in the outer layer," *Physics of Fluids*, Vol. 11, No. 2, 1999, pp. 417–422. https://doi.org/10.1063/1.869889.
- [4] Dennis, D. J. C., and Nickels, T. B., "Experimental measurement of large-scale three-dimensional structures in a turbulent boundary layer. Part 2. Long Structures," *Journal of Fluid Mechanics*, Vol. 673, 2011, pp. 218–244. https://doi.org/10.1017/ S0022112010006324.
- [5] Jiménez, J., "Coherent structures in wall-bounded turbulence," *Journal of Fluid Mechanics*, Vol. 842, 2018, p. P1. https://doi.org/10.1017/jfm.2018.144.
- [6] Hutchins, N., and Marusic, I., "Evidence of very long meandering features in the logarithmic region of turbulent boundary layers," *Journal of Fluid Mechanics*, Vol. 579, 2007, pp. 1–28.
- [7] Adrian, R. J., "Hairpin vortex organization in wall turbulence," *Physics of Fluids*, Vol. 19, No. 4, 2007, p. 41301. https://doi.org/10.1063/1.2717527.
- [8] Sahlin, A., Johansson, A. V., and Alfredsson, P. H., "The possibility of drag reduction by outer layer manipulators in turbulent boundary layers," *The Physics of Fluids*, Vol. 31, No. 10, 1988, pp. 2814–2820. https://doi.org/10.1063/1.866989.
- [9] Virk, P. S., Merrill, E., Mickley, H., Smith, K., and Mollo-Christensen, E., "The Toms phenomenon: turbulent pipe flow of dilute polymer solutions," *Journal of Fluid Mechanics*, Vol. 30, No. 2, 1967, pp. 305–328.
- [10] Jiménez, J., "Turbulent flows over rough walls," Annu. Rev. Fluid Mech., Vol. 36, 2004, pp. 173-196.
- [11] Bushnell, D. M., Viscous drag reduction in boundary layers, Vol. 123, AIAA, 1990.
- [12] Walsh, M., and Lindemann, A., "Optimization and application of riblets for turbulent drag reduction," 22nd aerospace sciences meeting, 1984, p. 347.
- [13] Abbassi, M., Baars, W., Hutchins, N., and Marusic, I., "Skin-friction drag reduction in a high-Reynolds-number turbulent boundary layer via real-time control of large-scale structures," *International Journal of Heat and Fluid Flow*, Vol. 67, 2017, pp. 30–41.
- [14] Proctor, J. L., Brunton, S. L., and Kutz, J. N., "Dynamic mode decomposition with control," *SIAM Journal on Applied Dynamical Systems*, Vol. 15, No. 1, 2016, pp. 142–161.
- [15] Tsolovikos, A., Suryanarayanan, S., Bakolas, E., and Goldstein, D., "Model Predictive Control of Material Volumes with Application to Vortical Structures," *AIAA Journal*, Vol. 59, No. 10, 2021, pp. 4057–4070. https://doi.org/10.2514/1.J060413.
- [16] Tsolovikos, A., Jariwala, A., Suryanarayanan, S., Bakolas, E., and Goldstein, D., "Separation delay in turbulent boundary layers via model predictive control of large-scale motions," *Physics of Fluids*, Vol. 35, No. 11, 2023, p. 115118.
- [17] Lee, J., Lee, J. H., Choi, J.-I., and Sung, H. J., "Spatial organization of large-and very-large-scale motions in a turbulent channel flow," *Journal of fluid mechanics*, Vol. 749, 2014, pp. 818–840.
- [18] Eitel-Amor, G., Örlü, R., Schlatter, P., and Flores, O., "Hairpin vortices in turbulent boundary layers," *Physics of Fluids*, Vol. 27, No. 2, 2015, p. 025108.
- [19] Matsuura, K., "Hairpin vortex generation around a straight vortex tube in a laminar boundary-layer flow," *arXiv preprint* arXiv:1808.06510, 2018.
- [20] Jariwala, A., Tsolovikos, A., Suryanarayanan, S., Goldstein, D. B., and Bakolas, E., "On the effect of manipulating Large Scale Motions in a Boundary Layer," *AIAA AVIATION 2022 Forum*, 2022, p. 3771.
- [21] Acarlar, M. S., and Smith, C. R., "A study of hairpin vortices in a laminar boundary layer. Part 1. Hairpin vortices generated by hemisphere protuberances," *J. Fluid Mech*, Vol. 175, 1987, pp. 1–41. https://doi.org/10.1017/S0022112087000272.

- [22] Acarlar, M. S., and Smith, C. R., "A study of hairpin vortices in a laminar boundary layer. Part 2. Hairpin vortices generated by fluid injection," *Journal of Fluid Mechanics*, Vol. 175, 1987, pp. 43–83. https://doi.org/10.1017/S0022112087000284.
- [23] Haidari, A. H., and Smith, C. R., "The generation and regeneration of single hairpin vortices," *Journal of Fluid Mechanics*, Vol. 277, 1994, pp. 135–162.
- [24] Jabbal, M., and Zhong, S., "The near wall effect of synthetic jets in a boundary layer," *International Journal of Heat and Fluid Flow*, Vol. 29, 2008, pp. 119–130. https://doi.org/10.1016/j.ijheatfluidflow.2007.07.011.
- [25] Jariwala, A., Tsolovikos, A., Suryanarayanan, S., Bakolas, E., and Goldstein, D., "Effect of controlling the Large-Scale Motions on the Separation Region," *Bulletin of the American Physical Society*, 2022.
- [26] Tsolovikos, A., Jariwala, A., Suryanarayanan, S., Bakolas, E., and Goldstein, D., "Separation Delay in Turbulent Boundary Layers via Model Predictive Control of Large-Scale Motions," *Bulletin of the American Physical Society*, 2022.
- [27] Gildersleeve, S., Leong, C. M., and Amitay, M., "Interactions of a low aspect ratio dynamic pin with a laminar boundary layer," 45th AIAA Fluid Dynamics Conference, 2015, p. 2634.
- [28] Gildersleeve, S., and Amitay, M., "Three-dimensional wake characteristics associated with the jet assisted surface mounted actuator," 2018 Flow Control Conference, 2018, p. 3060.
- [29] Corke, T. C., Enloe, C. L., and Wilkinson, S. P., "Dielectric barrier discharge plasma actuators for flow control," *Annual review of fluid mechanics*, Vol. 42, 2010, pp. 505–529.
- [30] Wylie, J., Jariwala, A., Suryanarayanan, S., Goldstein, D., and Amitay, M., "Hairpin vortex generation for physio-cyber simulations and control," *Bulletin of the American Physical Society*, 2023.
- [31] Suzuki, T., and Yamamoto, F., "Hierarchy of hybrid unsteady-flow simulations integrating time-resolved PTV with DNS and their data-assimilation capabilities," *Fluid Dynamics Research*, Vol. 47, No. 5, 2015, p. 051407.
- [32] Skamarock, W. C., Klemp, J. B., Dudhia, J., Gill, D. O., Barker, D. M., Wang, W., and Powers, J. G., "A description of the advanced research WRF version 2," Tech. rep., National Center For Atmospheric Research Boulder Co Mesoscale and Microscale . . . , 2005.
- [33] Appelbaum, J., Ohno, D., Rist, U., and Wenzel, C., "DNS of a turbulent boundary layer using inflow conditions derived from 4D-PTV data," *Experiments in Fluids*, Vol. 62, 2021, pp. 1–21.
- [34] Druault, P., Lardeau, S., Bonnet, J.-P., Coiffet, F., Delville, J., Lamballais, E., Largeau, J.-F., and Perret, L., "Generation of three-dimensional turbulent inlet conditions for large-eddy simulation," *AIAA journal*, Vol. 42, No. 3, 2004, pp. 447–456.
- [35] de Silva, C. M., Philip, J., and Marusic, I., "Minimization of divergence error in volumetric velocity measurements and implications for turbulence statistics," *Experiments in fluids*, Vol. 54, 2013, pp. 1–17.
- [36] Wang, C., Gao, Q., Wang, H., Wei, R., Li, T., and Wang, J., "Divergence-free smoothing for volumetric PIV data," *Experiments in Fluids*, Vol. 57, 2016, pp. 1–23.
- [37] Diamond, S., and Boyd, S., "CVXPY: A Python-embedded modeling language for convex optimization," The Journal of Machine Learning Research, Vol. 17, No. 1, 2016, pp. 2909–2913.
- [38] Paul F. Fischer, J. W. L., and Kerkemeier, S. G., "nek5000 Web page,", 2008. Http://nek5000.mcs.anl.gov.